

See discussions, stats, and author profiles for this publication at: <https://www.researchgate.net/publication/368550284>

# Realization of Zero-Field Skyrmions in a Magnetic Tunnel Junction

Article in *Advanced Electronic Materials* · February 2023

DOI: 10.1002/aelm.202201240

CITATIONS

4

READS

205

17 authors, including:



**Bin He**

Chinese Academy of Sciences

10 PUBLICATIONS 40 CITATIONS

[SEE PROFILE](#)



**Yue hu**

Lanzhou University

10 PUBLICATIONS 391 CITATIONS

[SEE PROFILE](#)



**Chenbo Zhao**

Lanzhou University of Technology

32 PUBLICATIONS 244 CITATIONS

[SEE PROFILE](#)



**Yu Zhang**

Chinese Academy of Sciences

30 PUBLICATIONS 217 CITATIONS

[SEE PROFILE](#)

# Realization of Zero-Field Skyrmions in a Magnetic Tunnel Junction

Bin He, Yue Hu, Chenbo Zhao, Jinwu Wei, Junwei Zhang, Yu Zhang, Chen Cheng, Jiahui Li, Zhuyang Nie, Yanxiang Luo, Yan Zhou, Shilei Zhang, Zhongming Zeng, Yong Peng, John Michael David Coey, Xiufeng Han, and Guoqiang Yu\*

Magnetic skyrmions are topologically protected noncollinear spin textures, which are regarded as promising information carriers for next-generation spintronic devices due to their small size and the low current density needed to drive their motion. Stability of skyrmions in zero external magnetic field is important for promoting fundamental studies and device applications. A few zero-field skyrmion-hosting materials have been developed, but none of them have been successfully integrated into a magnetic tunnel junction (MTJ), a crucial device for converting skyrmion information into an electrical signal. Here, a zero-field exchange-biased skyrmion material is developed and incorporated into an MTJ device. An Ir layer is inserted between the antiferromagnetic and ferromagnetic layers, which plays a crucial role in prohibiting interlayer diffusion under thermal annealing, resulting in simultaneous enhancement of exchange bias and thermal stability. The smallest zero-field skyrmions have a size of 100 nm at room temperature. The zero-field skyrmion material is then integrated into a perpendicularly magnetized MTJ, leading to the first demonstration of zero-field skyrmions in an MTJ, which is an important step toward developing skyrmion-based spintronic devices.

## 1. Introduction

Magnetic skyrmions are topologically protected particle-like swirling spin textures that have potential applications as information carriers in racetrack memory,<sup>[1]</sup> logic,<sup>[2,3]</sup> and synaptic computing<sup>[4,5]</sup> due to their nanometer scale and ultralow threshold driving current.<sup>[6]</sup> Skyrmions have been observed in bulk non-centrosymmetric magnets<sup>[7–14]</sup> and thin-film heterostructures with interfacial symmetry breaking.<sup>[15–17]</sup> The thin-film heterostructures formed by stacking layers of magnetic and non-magnetic metals possess an interfacial Dzyaloshinskii–Moriya interaction (DMI), which can create sub-hundred-nanometer Néel-type skyrmions at room temperature in cooperation with dipolar interaction, magnetic anisotropy, and Zeeman energy.<sup>[18–20]</sup> These material systems offer a unique platform for the further development of skyrmion-based

B. He, C. Zhao, J. Wei, Y. Zhang, C. Cheng, J. Li, Z. Nie, X. Han, G. Yu  
 Beijing National Laboratory for Condensed Matter Physics  
 Institute of Physics  
 Chinese Academy of Sciences  
 Beijing 100190, China  
 E-mail: guoqiangyu@iphy.ac.cn

B. He, Y. Zhang, C. Cheng, J. Li, Z. Nie, X. Han, G. Yu  
 Center of Materials Science and Optoelectronics Engineering  
 University of Chinese Academy of Sciences  
 Beijing 100049, China

Y. Hu, J. Zhang, Y. Peng  
 Key Laboratory for Magnetism and Magnetic Materials  
 of Ministry of Education  
 Lanzhou University  
 Lanzhou 730000, China

C. Zhao, Y. Zhou  
 School of Science and Engineering  
 The Chinese University of Hong Kong  
 Shenzhen 518172, China


Y. Luo, Z. Zeng  
 Nanofabrication Facility  
 Suzhou Institute of Nano-Tech and Nano-Bionics Chinese  
 Academy of Sciences Suzhou  
 Jiangsu 215123, China

S. Zhang  
 School of Physical Science and Technology  
 ShanghaiTech University  
 Shanghai 201210, China

S. Zhang  
 ShanghaiTech Laboratory for Topological Physics  
 ShanghaiTech University  
 Shanghai 200031, China

J. M. D. Coey  
 CRANN, AMBER and School of Physics  
 Trinity College Dublin  
 Dublin 2, Ireland

X. Han, G. Yu  
 Songshan Lake Materials Laboratory  
 Dongguan, Guangdong 523808, China

 The ORCID identification number(s) for the author(s) of this article can be found under <https://doi.org/10.1002/aelm.202201240>.

© 2023 The Authors. Advanced Electronic Materials published by Wiley-VCH GmbH. This is an open access article under the terms of the Creative Commons Attribution License, which permits use, distribution and reproduction in any medium, provided the original work is properly cited.

DOI: 10.1002/aelm.202201240

devices, such as a skyrmion shift device,<sup>[20–22]</sup> a skyrmion reshuffler device,<sup>[23]</sup> and skyrmion-based artificial synapses.<sup>[24]</sup> The realization of electrical generation, deletion, shift, and read-out functions are the basic prerequisites for the application of these devices. Up to now, approaches employed for skyrmion generation and deletion functions include using current-induced spin-orbit torque,<sup>[15,17,22,25–27]</sup> magnetic field,<sup>[17,18,20]</sup> and electrical field<sup>[28,29]</sup> The skyrmion shift function has also been realized by current-induced spin-orbit torque.<sup>[15,17,19–21,30]</sup> As for skyrmion read-out, topological Hall effect,<sup>[6,31,32]</sup> anomalous Hall effect,<sup>[33,34]</sup> and anomalous Nernst effect<sup>[35,36]</sup> have been used to detect skyrmions electrically. However, the electrical signal corresponding to one skyrmion is quite small. A promising alternative is tunneling magnetoresistance (TMR) implemented in a magnetic tunnel junction (MTJ) due to the extraordinarily large electrical response when the magnetization changes<sup>[37–40]</sup> and compatibility with the current semiconductor processing.<sup>[41]</sup> Using an MTJ for skyrmion read-out seems to be the most promising route to develop skyrmion-based devices.

On the other hand, an external magnetic field is commonly required to stabilize the skyrmions, which hampers device applications due to the increase in complexity needed to implement a magnetic field in the devices. This difficulty can be overcome by utilizing interlayer exchange coupling,<sup>[42]</sup> confined geometries,<sup>[19,43]</sup> exchange bias (EB),<sup>[44,45]</sup> and magnetic history control.<sup>[46]</sup> Among these schemes, use of EB to replace the external magnetic field shows great potential for device applications because EB materials have been extensively employed in spintronic devices, such as the MTJs. In an exchange-biased multilayer, EB<sup>[44]</sup> perpendicular magnetic anisotropy (PMA)<sup>[47]</sup> and DMI<sup>[48]</sup> can be finely tuned, and zero-field skyrmions can be stabilized.<sup>[44,45]</sup> Although very promising, there are two challenges to incorporate the present exchange-biased materials into the devices. On the one hand, the interfacial DMI of the CoFeB-based exchange-biased system is relatively weak,<sup>[48]</sup> which hampers the reduction of room-temperature skyrmion size.<sup>[49]</sup> On the other hand, the ferromagnet/antiferromagnet interface usually degrades on high-temperature annealing,<sup>[50,51]</sup> which is detrimental to MTJ integration because post-annealing is needed to improve the TMR. Because of these difficulties, zero-field exchange bias skyrmion materials have not yet been employed in MTJ devices.

In this work, we develop the exchange-biased stacks, namely IrMn/Ir( $t_{\text{Ir}}$ )/CoFeB/MgO, in which skyrmion can be stabilized by the exchange bias at zero field. The thin Ir insertion layer simultaneously enhances the magnitude and thermal stability of the EB. By increasing the multilayer repetition number, we can obtain hundred-nanometer scale zero-field skyrmions. More importantly, the exchange-biased multilayer is successfully integrated into MTJs. Our work may promote the development of skyrmion-based devices with MTJs for read-out.

## 2. Results and Discussion

The sample structure used in this work is as follows:

Sample series I: Ta (3)/Ir<sub>22</sub>Mn<sub>78</sub> (6.7)/Ir ( $t_{\text{Ir}}$ )/Co<sub>20</sub>Fe<sub>60</sub>B<sub>20</sub> (1.1)/MgO (1)/Ta (2) ( $t_{\text{Ir}}$  = 0–1.0, thicknesses in nanometers, the numbers in brackets represent the thickness)

Sample II: Ta (3)/IrMn (6.7)/Ir (0.4)/CoFeB (wedge)/MgO (1)/Ta (2)

Sample series III: Ta (3)/[IrMn (5)/Ir (0.4)/CoFeB (1.4)/MgO (1)]<sub>N</sub>/Ta (2) ( $N$  = 3, 5, 7, 9, and 11, which refer to the repetition numbers of multilayer)

Sample series IV: Ta (2)/[Ta (1)/Ir (2)/CoFeB (1.1)/MgO (1)]<sub>N</sub>/Ta (2)

Sample V: Ta (5)/IrMn (6.7)/Ir (0.4)/CoFeB (wedge) (free layer, is also skyrmion layer)/MgO (1.3)/CoFeB (1.4) (reference layer)/Ta (0.5)/[Pt (0.5)/Co (0.5)]<sub>5</sub>/Ir (0.5)/[Pt (0.5)/Co (0.5)]<sub>5</sub> (pinning layer)/Ta (2)

### 2.1. Enhancement of Exchange Bias

A sample stack series I is shown in **Figure 1a**. The thin Ir insertion layer is used to enhance the exchange bias coupling strength and thermal stability. Meantime, the Ir/CoFeB interface possesses a stronger interfacial DMI compared to IrMn/CoFeB interface, as suggested by the previous research,<sup>[48]</sup> which is helpful for stabilizing small skyrmions. The influence of thermal annealing on the exchange bias was studied first. **Figure 1b** shows the out-of-plane magnetic hysteresis ( $M$ – $H$ ) loops of the as-grown and annealed samples (see all the hysteresis loops in Section S1, Supporting Information). All the as-grown samples show PMA. However, the PMA and EB vanish after annealing at temperatures above 250 °C for the sample without the Ir insertion layer. By contrast, the EB is preserved for the samples with  $t_{\text{Ir}}$  = 0.6 nm after 250 °C annealing. The difference in microscopic structure between the samples with and without the Ir insertion layer is revealed by transmission electron microscopy (TEM) images and energy-dispersive X-ray elemental mapping, as shown in **Figure 1c,d**. For the sample without the Ir insertion layer, the diffusion of Mn atoms degrades the IrMn/CoFeB and CoFeB/MgO interfaces and hence the EB and PMA. On the contrary, for the sample with  $t_{\text{Ir}}$  = 0.6 nm, the diffusion of Mn is suppressed, and clear, sharp interfaces are retained, which is the key to sustain the EB and PMA and reduce the magnetic dead layer (see Section S2, Supporting Information). We further extract the  $H_{\text{eb}}$  as a function of  $t_{\text{Ir}}$  at different annealing temperatures, as shown in **Figure 1e**. It shows a non-monotonic dependence on  $t_{\text{Ir}}$  and has a maximum at  $t_{\text{Ir}}$  = 0.4 nm for both as-grown and annealed samples. Such an enhancement of EB with an appropriate Ir layer thickness may be a consequence of the change of chemical composition at the IrMn/Ir interface, which has been demonstrated to have a significant effect on the exchange bias.<sup>[52,53]</sup> In addition, the  $H_{\text{eb}}$  disappears when the Ir insertion layer is thicker than 0.8 nm for the as-grown samples (black curve). However, the  $H_{\text{eb}}$  remains 4 Oe when  $t_{\text{Ir}}$  = 1.0 nm for the 250 °C annealed sample. This may be due to the diffusion of Mn atoms into the Ir layer to form an IrMn alloy and produce a weak EB.

### 2.2. Evaluation of Gilbert Damping

We also evaluate the Gilbert damping constant  $\alpha$  of the exchange-biased samples because it is a crucial factor in determining the performance of skyrmion-based devices<sup>[30]</sup> and

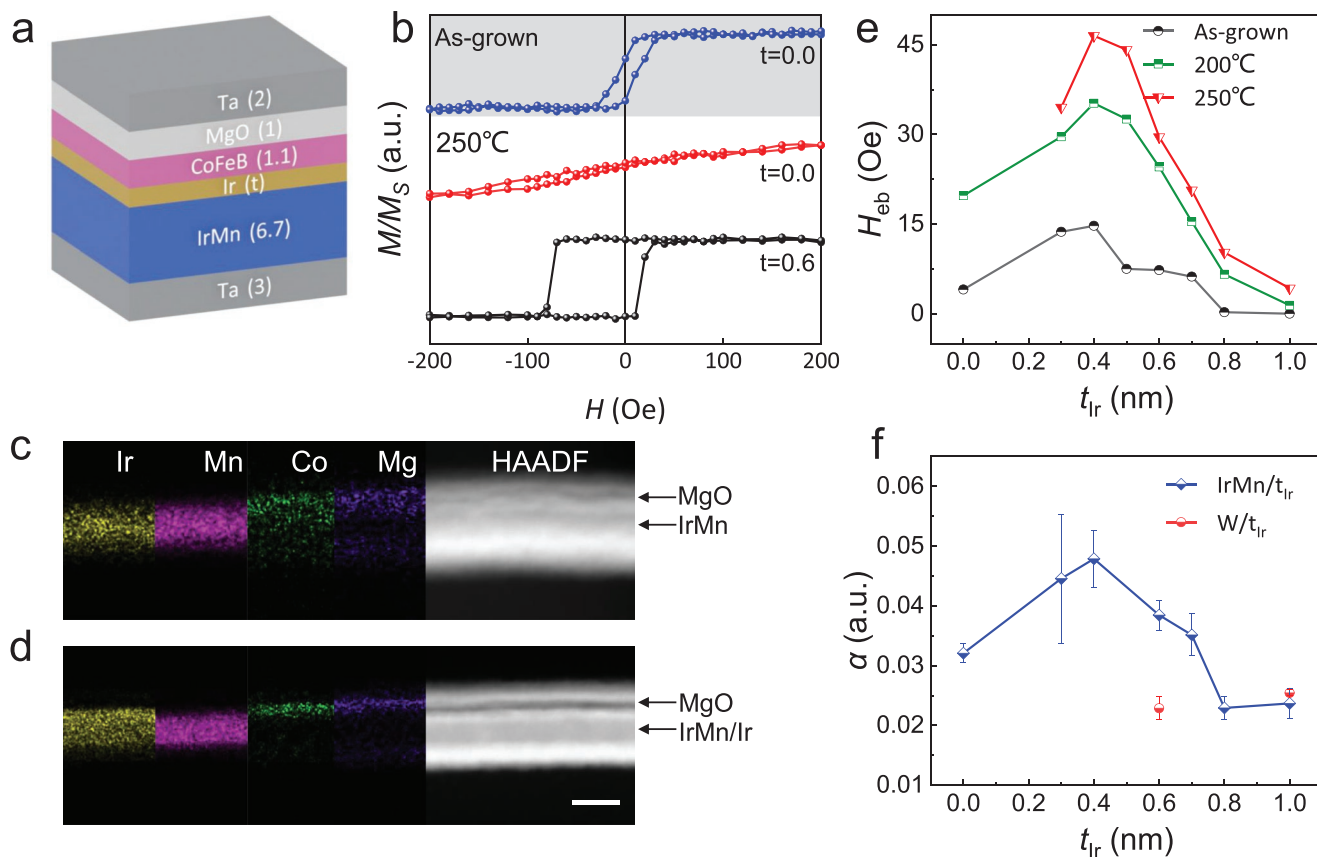


**Figure 1.** Enhanced exchange bias and ST-FMR measurement. a) The experimental sample structure: Ta (3)/Ir<sub>22</sub>Mn<sub>78</sub> (6.7)/Ir (*t<sub>Ir</sub>*)/Co<sub>20</sub>Fe<sub>60</sub>B<sub>20</sub> (1.1)/MgO (1)/Ta (2). b) Out-of-plane magnetic hysteresis loops of different *t<sub>Ir</sub>* for the as-grown and 250 °C annealed samples. Energy-dispersive X-ray elemental mapping of Ir, Mn, Co, and Mg and a scanning transmission-electron-microscopy image of a cross section of the sample obtained in a high-angle annular dark-field imaging mode. c) Sample without Ir insertion layer annealed at 250 °C. d) Sample with *t<sub>Ir</sub>* = 0.6 nm annealed at 250 °C. All scale bars: 10 μm. e) Enhanced exchange bias field as a function of *t<sub>Ir</sub>* for the as-grown sample and the samples annealed at 200 and 250 °C. f) Gilbert damping constant  $\alpha$  as a function of *t<sub>Ir</sub>*.

it is usually correlated with the exchange bias.<sup>[54,55]</sup> Here we use spin-torque ferromagnetic resonance (ST-FMR) to study the dynamic magnetic properties of the enhanced EB system<sup>[56]</sup> (see the details of ST-FMR setup in Section S3, Supporting Information). Figure 1f shows  $\alpha$  as a function of *t<sub>Ir</sub>* for IrMn-based and W-based systems. The structure of the W-based system is W (3)/CoFeB (1.1)/MgO (1)/W (2) and designed as a control sample due to its lack of exchange bias coupling. We observe that  $\alpha$  is smaller in the W-based sample than that of the exchange-biased sample with the same thickness of Ir insertion layer even though the spin pumping-induced damping increase should be more significant because of the large spin Hall angle of W.<sup>[57,58]</sup> On the other hand,  $\alpha$  of the IrMn-based sample exhibits a similar variation trend to the EB. These behaviors indicate that the increase of  $\alpha$  in the exchange-biased system is closely related to the exchange bias coupling.<sup>[54,55]</sup> Despite the increase of  $\alpha$  due to the EB, we want to emphasize that the studied exchange-biased system is suitable as MgO-based MTJ ferromagnetic electrodes.

### 2.3. Zero-Field Skyrmions

Based on the developed exchange-biased system, we further design the zero-field skyrmion samples, including sample II,

sample series III, and control sample series IV. Here, sample II is used to facilitate the zero-field skyrmions. Sample series III and IV are used to further reduce the skyrmion diameter and as control samples, respectively. In the exchange-biased samples, the Ir insertion layer of *t<sub>Ir</sub>* = 0.4 nm is chosen because it leads to the largest  $H_{\text{eb}}$ . A wedged CoFeB layer in sample II is used to tune PMA to facilitate skyrmion formation. Thereafter, sample II is annealed at 250 °C with an out-of-plane field to enhance PMA and introduce a uniform EB. **Figure 2a** shows the hysteresis loop of sample II, which is measured in a polar magneto-optical Kerr effect (p-MOKE) microscope. The p-MOKE images of sample II in **Figure 2b–d** depict the evolution of magnetic domain patterns with the out-of-plane magnetic field. A stable skyrmion phase appears when the magnetic field decreases from negative maximum to zero, as shown in **Figure 2b**. The diameter of the skyrmion marked by the red dotted circle in **Figure 2b** is  $520 \pm 15$  nm. We note that the size of skyrmions is mainly distributed in a wide range of 500 nm–2 μm, which may be due to the inhomogeneity of film thickness, impurities, defects, and EB.<sup>[44]</sup> On increasing the magnetic field to 32 Oe, the skyrmions expand and transform into a multidomain structure (**Figure 2c**). When the magnetic field decreases from a positive maximum to 39 Oe, skyrmions with opposite polarity appear, as shown in **Figure 2d**.

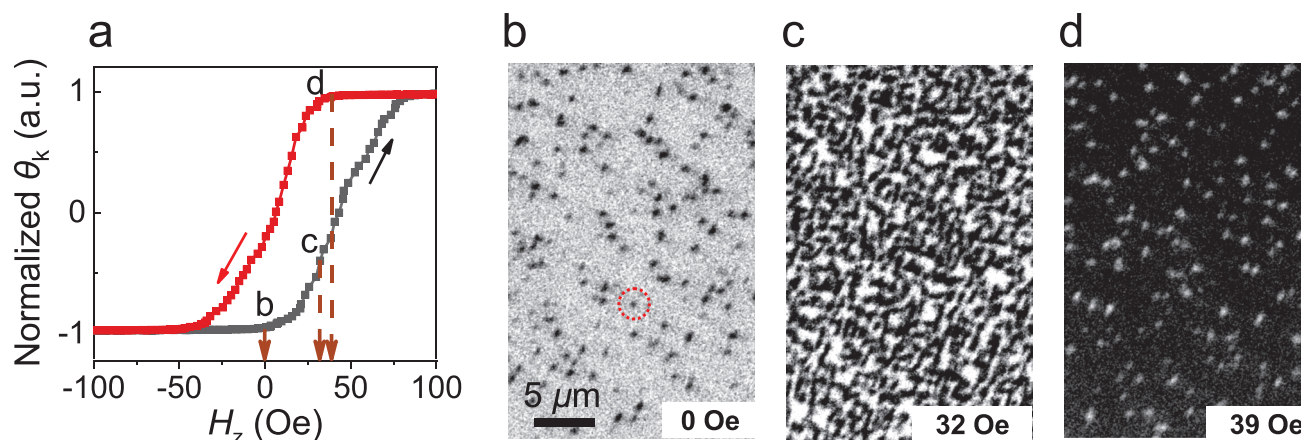


**Figure 2.** Zero-field skyrmions. a) The hysteresis loop of Ta (3)/IrMn (6.7)/Ir (0.4)/CoFeB (wedge)/MgO (1)/Ta (2) measured by p-MOKE. The colored arrows represent the different sweeping directions of the magnetic field. b–d) P-MOKE images at different out-of-plane magnetic fields. The skyrmion diameter marked by the red dotted circle is  $520 \pm 15$  nm. The bright (dark) areas represent  $M_z < 0$  ( $M_z > 0$ ).

#### 2.4. The Effect of Dipolar Interaction on Domain Periodicity

The skyrmion size is usually decreased by increasing dipolar interaction.<sup>[18]</sup> Here the sample series III was first annealed in the absence of a magnetic field to exclude the influence of EB. The  $M$ – $H$  loops indicate that all samples exhibit a strong PMA signal (see Figures S4 and S5, Supporting Information). Figure 3a–c show the zero-field Lorentz transmission electron microscopy (LTEM) images at a tilt angle of  $30^\circ$  for the samples series III with  $N = 3, 7,$  and  $11$  after AC demagnetization in an out-of-plane field, respectively (for other LTEM images, see Figure S6, Supporting Information). All images show a typical labyrinth domain structure. The domain periodicity is extracted as a function of repetition  $N$ , as shown in Figure 3d (see Figure S9, Supporting Information for the method of getting domain periodicity from LTEM images). The domain periodicity first shows a slight decrease and then an increase with the increase of  $N$  in IrMn-based samples, which is mainly a result of the variation of dipolar interaction. By contrast, the dependence of domain periodicity on repetition  $N$  exhibits a trend of decrease in the Ir-based multilayer, allowing to realize an even smaller skyrmion size. The domain periodicity will likely reach a minimum point and then increase like the IrMn-based multilayer, as suggested by previous work.<sup>[59–61]</sup> The difference in the smallest skyrmion size and the corresponding repetition number between the two samples is likely due to the difference in the dipolar field between the two samples since different CoFeB layer thicknesses are used. This fact also suggests that one may further reduce the skyrmion size by modulating the dipolar interaction.

#### 2.5. Hundred-Nanometer Zero-Field Skyrmions

We choose the sample of series III with  $N = 3$  to pursue the zero-field skyrmion because the skyrmion size does not vary obviously when  $N$  is larger than three (see Figure 3d) and the required magnetic field for stabilizing skyrmion is small for small  $N$  (see Figure S5, Supporting Information). Here we note that the sample of series III with  $N = 3$  is annealed at an

out-of-plane magnetic field to introduce a uniform EB. Figure 3e–g shows the corresponding zero-field LTEM images at different tilt angles  $-30^\circ, 0^\circ,$  and  $30^\circ$ , respectively. Obviously, the contrast asymmetry of the skyrmion with the green dotted circle reverses depending on the sign of the tilt, and it disappears at zero tilt, which demonstrates the existence of Néel-type skyrmions in this system.<sup>[62]</sup> The corresponding line profiles are shown in Figure 3h, showing that the skyrmion has a diameter of  $148.4 \pm 5.3$  nm. We notice that stripe domains gradually appear in the films, which may be due to the domain structures in the EB system being sensitive to the electron beam.<sup>[63]</sup>

#### 2.6. Skyrmions in the MTJ

Finally, we discuss the integration of the zero-field skyrmion material with the MTJ devices. The MTJ device stacks  $V$  is shown in Figure 4a. Figure 4b shows the  $M$ – $H$  loop of the MTJ film, which exhibits a clear antiferromagnetic coupling of the synthetic antiferromagnet (SAF) layers. The inset of Figure 4b is the minor  $M$ – $H$  loop, which corresponds to the flip of the magnetic moment of the free layer. Figure 4c,d shows the zero-field p-MOKE images for different sweeping histories of the MTJ film. The domain patterns at other magnetic fields are shown in Figure S7, Supporting Information. First, we saturate the film using a magnetic field of 3 kOe and then scan the field in the range from  $-200$  Oe to  $200$  Oe. A stable skyrmion phase can be observed in Figure 4c when the magnetic field increases from  $-200$  Oe to zero, which has a similar size distribution to Figure 2b. In contrast, a multidomain state is formed when the magnetic field returns from  $200$  Oe to zero (Figure 4d). The fuzzy domain structures in Figure 4c,d are mainly because the covering layers on top of the CoFeB layer reduce the contrast of the magnetic textures.

The TMR loop and corresponding magnetic configuration of magnetic layers are shown in Figure 4e. With decreasing field from 2 kOe (see black curve), the two parallel magnetic moments of SAF layers (see blue and yellow arrows) gradually evolve to antiferromagnetic coupling, corresponding to a little abrupt jump in the black curve. With further changing the

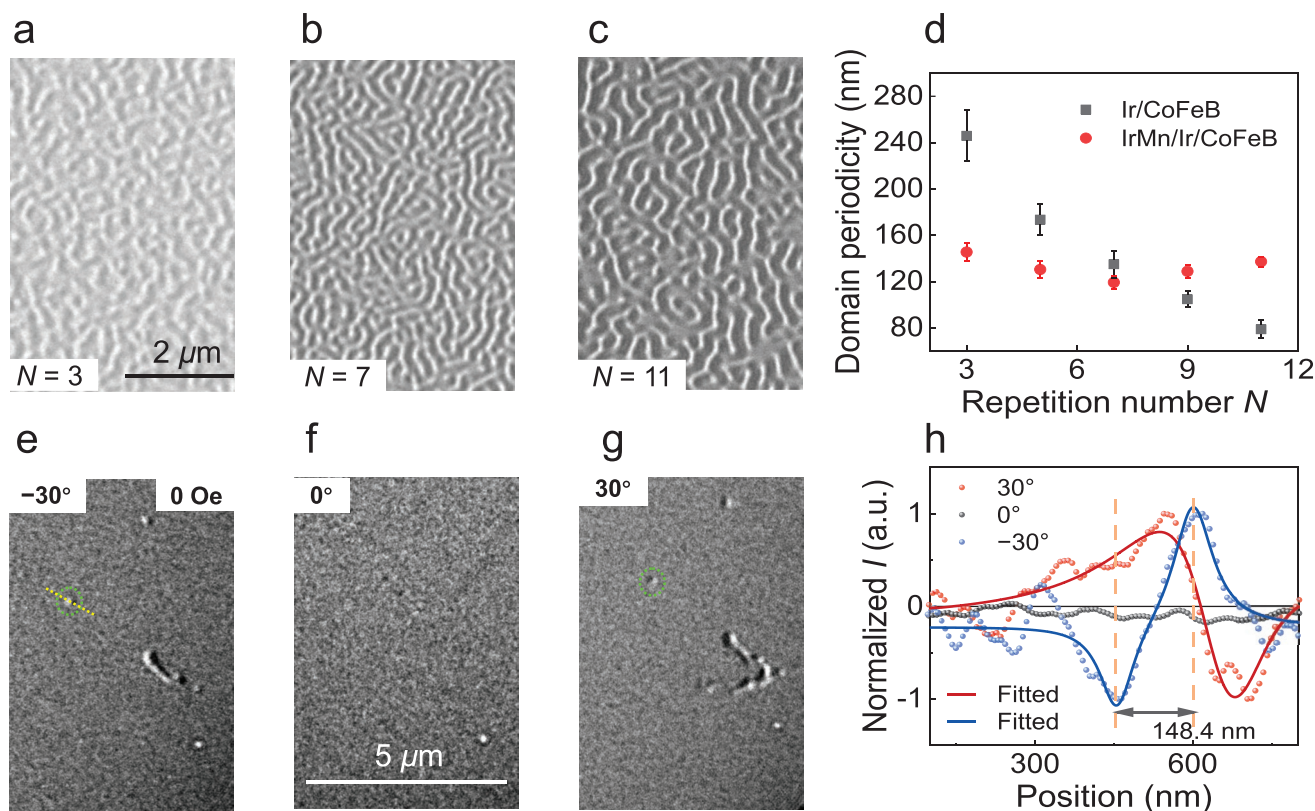


**Figure 3.** The effect of dipolar interaction on domain periodicity and hundred-nanometer zero-field skyrmions. a–c) The zero-field domain pattern captured by LTEM after AC demagnetization in an out-of-plane field for Ta (3)/IrMn (5)/Ir (0.4)/CoFeB (1.4)/MgO (1)<sub>N</sub>/Ta (2),  $N = 3$  (a),  $N = 7$  (b), and  $N = 11$  (c), respectively. d) The domain periodicity of Ta (3)/IrMn (5)/Ir (0.4)/CoFeB (1.4)/MgO (1)<sub>N</sub>/Ta (2) (black dot) and Ta (2)/Ta (1)/Ir (2)/CoFeB (1.1)/MgO (1)<sub>N</sub>/Ta (2) (red dot) ( $N = 3, 5, 7, 9$ , and 11) extracted from LTEM images as a function of repetition number  $N$ . e–g) LTEM images of Ta (3)/IrMn (5)/Ir (0.4)/CoFeB (1.4)/MgO (1)<sub>3</sub>/Ta (2) with tilt angles of  $-30^\circ$ ,  $0^\circ$ , and  $30^\circ$ , which were obtained at zero field. The green dotted circle indicates the skyrmion at zero field. h) Line profiles (colored points) and fitted curves (colored lines) of a skyrmion with a diameter of 148.4 nm extracted from (e–g).

magnetic field to  $-1$  kOe, the free layer is progressively flipped, and a parallel state is obtained. Hence, the resistance gradually drops and eventually reaches the low-resistance state. We note that the magnetic moments of SAF layers are still aligned antiparallel since the external field (1 kOe) cannot overcome the antiferromagnetic coupling of SAF, which is consistent with Figure 4b. After reversing the field (see red curve), the reversal of the free layer occurs at 30 Oe, leading to the increase of the resistance. The TMR is about 22.6%. We note that the low TMR when the field is swept from the positive direction to zero is likely due to the imperfect antiparallel magnetic configuration. Similarly, the low TMR appears when the magnetic field is swept from 2 kOe to zero (see Figure S8, Supporting Information).

We now focus on the minor TMR loop, in which only the CoFeB free layer is flipped, as shown in Figure 4f. The switching polarity depends on the initial magnetization state of the reference layer because of the different orientations of the reference layer. We notice that the two different minor loops have different  $H_{\text{eb}}$ . It is  $-55.8$  Oe ( $H_{\text{eb1}}$ ) after saturation in 3 kOe (see black curve) and  $-39.1$  Oe ( $H_{\text{eb2}}$ ) after saturation in  $-3$  kOe (see red curve). The difference in EB of the minor  $R$ - $H$  loops is most likely caused by the dipolar field  $|H_{\text{d}}|$  of the reference layer. The direction of  $H_{\text{d}}$  is downward (upward) when the saturation field  $H_{\text{s}}$  equals 3 kOe

( $-3$  kOe). Note that the direction of  $H_{\text{eb}}$  is downward. Therefore, the  $H_{\text{eb}}$  due to the exchange bias can be expressed as  $H_{\text{eb}} = H_{\text{eb1}} - H_{\text{d}}$  for a saturation field of 3 kOe and  $H_{\text{eb}} = H_{\text{eb2}} + H_{\text{d}}$  for a saturation field of  $-3$  kOe. We find that  $|H_{\text{d}}|$  and  $H_{\text{eb}}$  is about 8.4 Oe and  $-475$  Oe, respectively. The magnitude of  $H_{\text{eb}}$  in the MTJ device is consistent with the result of thin films.

### 3. Conclusion

We have demonstrated that a thin Ir insertion layer between CoFeB and IrMn can enhance not only the EB but also the thermal stability. ST-FMR measurement indicates that the increase in exchange bias is accompanied by an increase in damping. LTEM images demonstrate the existence of hundred-nanometer scale zero-field skyrmions. By tailoring the repetition number, the domain periodicity and skyrmion size can be further modulated in an appropriate way. The most important thing is that we successfully integrate the zero-field skyrmion material system into the MTJs, which solves the difficulty of compatibility between zero-field skyrmion material and MTJ. This work may lead to a superior material system for skyrmion read-out and promote the development of skyrmion-based race-track memory in spintronics.

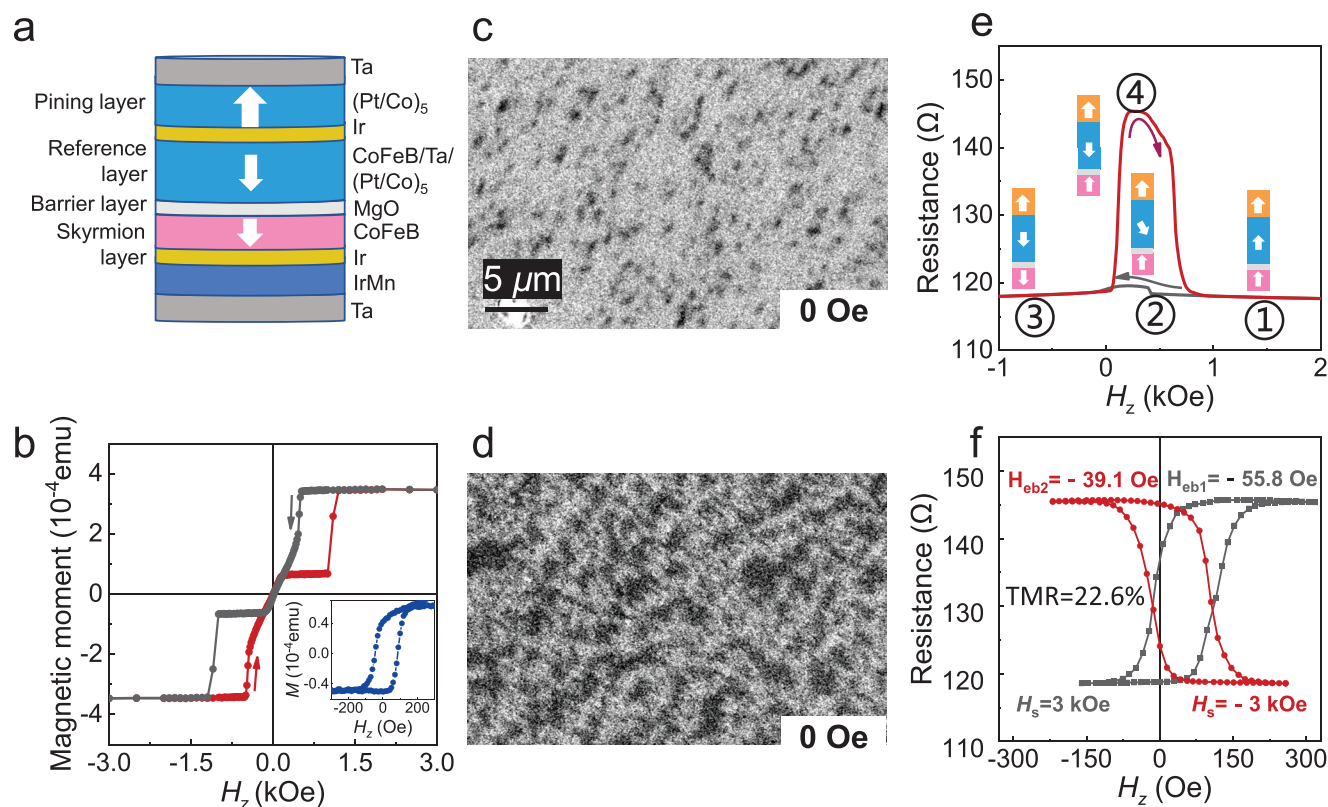


**Figure 4.** Skyrmions in the MTJ. a) The structure of MTJ films. From top to bottom layers are: [Pt (0.5)/Co (0.5)]<sub>5</sub>/Ir (0.5)/[Pt (0.5)/Co (0.5)]<sub>5</sub> (pinning layer), CoFeB (1.4) (reference layer), MgO (1.3) (barrier layer) and IrMn (6.7)/Ir (0.4)/CoFeB (wedge) (free layer, is also skyrmion layer), respectively. The white arrows represent the magnetic moment of the corresponding magnetic layers. b) Out-of-plane magnetic hysteresis loop of the MTJ film. The inset shows the minor loop, which corresponds to the flip magnetic moments of the free layer. c,d) Zero-field magnetic domain structures captured by p-MOKE at different sweeping directions of the magnetic field after saturation in  $-3$  kOe. e) Out-of-plane resistance hysteresis loop for the MTJ with a junction diameter of  $5 \mu\text{m}$ . The inset arrows refer to the magnetic configurations of the different layers at the different magnetic fields as labeled by numbers ①, ②, ③, ④. f) The minor resistance hysteresis loops for the MTJ with a TMR of 22.6%. The black (red) dotted line corresponds to the saturation field of 3 kOe ( $-3$  kOe).

## 4. Experimental Section

The samples were grown on silicon nitride membranes and a Si/SiO<sub>2</sub> substrate using a DC and RF magnetron sputtering system. The base pressure was less than  $8 \times 10^{-9}$  Torr. The Si/Si<sub>3</sub>N<sub>4</sub> membranes and Si/SiO<sub>2</sub> wafers were used as substrates for carrying out LTEM and MOKE measurements, respectively. The deposition pressure of the Ar gas was 9 mTorr for CoFeB and 3 mTorr for others, respectively. For the annealing sample, an out-of-plane field of 8 kOe was applied at 250 °C under  $3 \times 10^{-6}$  Torr for 30 min. The LTEM images were acquired in a FEI Titan Cs Probe TEM in Lorentz mode (the Fresnel imaging mode) with an acceleration voltage 300 kV. All images were obtained at a tilt angle 30° (unless mentioned), and defocus value was set as 600 μm. The direction of the magnetic field was parallel to the microscope's objective lens. The MTJ pillars were fabricated by means of standard photolithography and subsequent Ar ion milling. A SiO<sub>2</sub> (50 nm) layer was deposited to provide electrical insulation between the top and bottom electrodes. Finally, the electrodes with Pt (10)/Au (80) were deposited as the top and bottom electrodes using the lift-off process after photolithography.

## Supporting Information

Supporting Information is available from the Wiley Online Library or from the author.

## Acknowledgements

This work was financially supported by the National Key Research and Development Program of China (Grant No. 2022YFA1403602), the Science Center of the National Science Foundation of China (Grant No. 52088101), the Beijing Natural Science Foundation (Grant No. Z190009), the National Natural Science Foundation of China (Grant Nos. 12274437, 52161160334), the K. C. Wong Education Foundation (Grant No. GJTD-2019-14), the financial support of the Shenzhen Peacock Group Plan (Grant No. KQTD20180413181702403), and the Guangdong Special Support Project (2019BT02×030). The authors thank Prof. Jianwang Cai for the helpful discussion.

## Conflict of Interest

The authors declare no conflict of interest.

## Author Contributions

G.Y. conceived the project. B.H. prepared the samples, characterized the multilayer films, fabricated MTJ, performed ST-FMR measurement, and carried out the MOKE measurements with supports from C.Z., J.W., C.C., J.L., Y.L., S.Z., Z.Z., J.M.D.C., and X.H. Y.H. performed the

Lorentz TEM imaging experiments with supports from J.Z. and Y.P. Y.Z. performed the TEM imaging experiments. B.H. drafted the paper and all authors commented on the manuscript. The study was performed under the supervision of G.Y.

## Data Availability Statement

The data that support the findings of this study are available from the corresponding author upon reasonable request.

## Keywords

enhanced exchange bias, magnetic skyrmions, magnetic tunnel junctions, zero-field skyrmions

Received: November 14, 2022

Revised: December 20, 2022

Published online: February 15, 2023

- [1] A. Fert, V. Cros, J. Sampaio, *Nat. Nanotechnol.* **2013**, *8*, 152.
- [2] X. Zhang, M. Ezawa, Y. Zhou, *Sci. Rep.* **2015**, *5*, 9400.
- [3] S. Luo, M. Song, X. Li, Y. Zhang, J. Hong, X. Yang, X. Zou, N. Xu, L. You, *Nano Lett.* **2018**, *18*, 1180.
- [4] K. M. Song, J.-S. Jeong, B. Pan, X. Zhang, J. Xia, S. Cha, T.-E. Park, K. Kim, S. Finizio, J. N. E. Raabe, *Nat. Electron.* **2020**, *3*, 148.
- [5] Y. Huang, W. Kang, X. Zhang, Y. Zhou, W. J. N. Zhao, *Nanotechnology* **2017**, *28*, 08LT02.
- [6] N. Nagaosa, Y. Tokura, *Nat. Nanotechnol.* **2013**, *8*, 899.
- [7] F. Jonietz, S. Muehlbauer, C. Pfleiderer, A. Neubauer, W. Muenzer, A. Bauer, T. Adams, R. Georgii, P. Boeni, R. A. Duine, K. Everschor, M. Garst, A. Rosch, *Science* **2010**, *330*, 1648.
- [8] S. Muehlbauer, B. Binz, F. Jonietz, C. Pfleiderer, A. Rosch, A. Neubauer, R. Georgii, P. Boeni, *Science* **2009**, *323*, 915.
- [9] W. Muenzer, A. Neubauer, T. Adams, S. Muehlbauer, C. Franz, F. Jonietz, R. Georgii, P. Boeni, B. Pedersen, M. Schmidt, A. Rosch, C. Pfleiderer, *Phys. Rev. B* **2010**, *81*, 041203.
- [10] A. Neubauer, C. Pfleiderer, B. Binz, A. Rosch, R. Ritz, P. G. Niklowitz, P. Boeni, *Phys. Rev. Lett.* **2009**, *102*, 186602.
- [11] Y. Onose, Y. Okamura, S. Seki, S. Ishiwata, Y. Tokura, *Phys. Rev. Lett.* **2012**, *109*, 037603.
- [12] S. Seki, X. Z. Yu, S. Ishiwata, Y. Tokura, *Science* **2012**, *336*, 198.
- [13] X. Z. Yu, N. Kanazawa, Y. Onose, K. Kimoto, W. Z. Zhang, S. Ishiwata, Y. Matsui, Y. Tokura, *Nat. Mater.* **2011**, *10*, 106.
- [14] X. Z. Yu, Y. Onose, N. Kanazawa, J. H. Park, J. H. Han, Y. Matsui, N. Nagaosa, Y. Tokura, *Nature* **2010**, *465*, 901.
- [15] W. Jiang, P. Upadhyaya, W. Zhang, G. Yu, M. B. Jungfleisch, F. Y. Fradin, J. E. Pearson, Y. Tserkovnyak, K. L. Wang, O. J. S. Heinonen, S. G. E. te Velthuis, A. Hoffmann, *Science* **2015**, *349*, 283.
- [16] R. Juge, K. Bairagi, K. G. Rana, J. Vogel, M. Sall, D. Mailly, V. T. Pham, Q. Zhang, N. Sisodia, M. Foerster, L. Aballe, M. Belmeguenai, Y. Roussigne, S. Auffret, L. D. Buda-Prejbeanu, G. Gaudin, D. Ravelosona, O. Boulle, *Nano Lett.* **2021**, *21*, 2989.
- [17] G. Yu, P. Upadhyaya, X. Li, W. Li, S. K. Kim, Y. Fan, K. L. Wong, Y. Tserkovnyak, P. K. Amiri, K. L. Wang, *Nano Lett.* **2016**, *16*, 1981.
- [18] C. Moreau-Luchaire, C. Moutafis, N. Reyren, J. Sampaio, C. A. F. Vaz, N. Van Horne, K. Bouzehouane, K. Garcia, C. Deranlot, P. Warnicke, P. Wohlhüter, J. M. George, M. Weigand, J. Raabe, V. Cros, A. Fert, *Nat. Nanotechnol.* **2016**, *11*, 444.
- [19] O. Boulle, J. Vogel, H. Yang, S. Pizzini, D. de Souza Chaves, A. Locatelli, T. O. Mentès, A. Sala, L. D. Buda-Prejbeanu, O. Klein, M. Belmeguenai, Y. Roussigne, A. Stashkevich, S. M. Cherif, L. Aballe, M. Foerster, M. Chshiev, S. Auffret, I. M. Miron, G. Gaudin, *Nat. Nanotechnol.* **2016**, *11*, 449.
- [20] S. Woo, K. Litzius, B. Kruger, M. Y. Im, L. Caretta, K. Richter, M. Mann, A. Krone, R. M. Reeve, M. Weigand, P. Agrawal, I. Lemesch, M. A. Mawass, P. Fischer, M. Klau, G. S. Beach, *Nat. Mater.* **2016**, *15*, 501.
- [21] G. Yu, P. Upadhyaya, Q. Shao, H. Wu, G. Yin, X. Li, C. He, W. Jiang, X. Han, P. K. Amiri, K. L. Wang, *Nano Lett.* **2017**, *17*, 261.
- [22] W. Legrand, D. Maccariello, N. Reyren, K. Garcia, C. Moutafis, C. Moreau-Luchaire, S. Collin, K. Bouzehouane, V. Cros, A. Fert, *Nano Lett.* **2017**, *17*, 2703.
- [23] J. Zázvorka, F. Jakobs, D. Heinze, N. Keil, S. Kromin, S. Jaiswal, K. Litzius, G. Jakob, P. Virnau, D. Pinna, K. Everschor-Sitte, L. Rózsa, A. Donges, U. Nowak, M. Kläui, *Nat. Nanotechnol.* **2019**, *14*, 658.
- [24] K. M. Song, J.-S. Jeong, B. Pan, X. Zhang, J. Xia, S. Cha, T.-E. Park, K. Kim, S. Finizio, J. Raabe, J. Chang, Y. Zhou, W. Zhao, W. Kang, H. Ju, S. Woo, *Nat. Electron.* **2020**, *3*, 148.
- [25] S. Finizio, K. Zeissler, S. Wintz, S. Mayr, T. Weßels, A. J. Huxtable, G. Burnell, C. H. Marrows, J. Raabe, *Nano Lett.* **2019**, *19*, 7246.
- [26] S. Woo, K. M. Song, X. Zhang, M. Ezawa, Y. Zhou, X. Liu, M. Weigand, S. Finizio, J. Raabe, M.-C. Park, K.-Y. Lee, J. W. Choi, B.-C. Min, H. C. Koo, J. Chang, *Nat. Electron.* **2018**, *1*, 288.
- [27] F. Büttner, I. Lemesch, M. Schneider, B. Pfau, C. M. Günther, P. Hessler, J. Geilhufe, L. Caretta, D. Engel, B. Krüger, J. Viehhaus, S. Eisebitt, G. S. D. Beach, *Nat. Nanotechnol.* **2017**, *12*, 1040.
- [28] P.-J. Hsu, A. Kubetzka, A. Finco, N. Romming, K. von Bergmann, R. Wiesendanger, *Nat. Nanotechnol.* **2017**, *12*, 123.
- [29] M. Schott, A. Bernard-Mantel, L. Ranno, S. Pizzini, J. Vogel, H. Béa, C. Baraduc, S. Auffret, G. Gaudin, D. Givord, *Nano Lett.* **2017**, *17*, 3006.
- [30] A. Hrabec, J. Sampaio, M. Belmeguenai, I. Gross, R. Weil, S. M. Cherif, A. Stashkevich, V. Jacques, A. Thiaville, S. Rohart, *Nat. Commun.* **2017**, *8*, 15765.
- [31] A. Neubauer, C. Pfleiderer, B. Binz, A. Rosch, R. Ritz, P. G. Niklowitz, P. Boni, *Phys. Rev. Lett.* **2009**, *102*, 186602.
- [32] D. Liang, J. P. DeGrave, M. J. Stolt, Y. Tokura, S. Jin, *Nat. Commun.* **2015**, *6*, 8217.
- [33] D. Maccariello, W. Legrand, N. Reyren, K. Garcia, K. Bouzehouane, S. Collin, V. Cros, A. Fert, *Nat. Nanotechnol.* **2018**, *13*, 233.
- [34] K. Zeissler, S. Finizio, K. Shahbazi, J. Massey, F. Al Ma'Mari, D. M. Bracher, A. Kleibert, M. C. Rosamond, E. H. Linfield, T. A. Moore, J. Raabe, G. Burnell, C. H. Marrows, *Nat. Nanotechnol.* **2018**, *13*, 1161.
- [35] A. F. Scaroni, C. Barton, H. Corte-Leon, S. Sievers, X. K. Hu, F. Ajejas, W. Legrand, N. Reyren, V. Cros, O. Kazakova, H. W. Schumacher, *Phys. Rev. Lett.* **2021**, *126*, 077202.
- [36] Z. D. Wang, M. H. Guo, H. A. Zhou, L. Zhao, T. Xu, R. Tomasello, H. Bai, Y. Q. Dong, S. G. Je, W. L. Chao, H. S. Han, S. Lee, K. S. Lee, Y. Y. Yao, W. Han, C. Song, H. Q. Wu, M. Carpentieri, G. Finocchio, M. Y. Im, S. Z. Lin, W. J. Jiang, *Nat. Electron.* **2020**, *3*, 672.
- [37] S. Li, A. Du, Y. Wang, X. Wang, X. Zhang, H. Cheng, W. Cai, S. Lu, K. Cao, B. Pan, N. Lei, W. Kang, J. Liu, A. Fert, Z. Hou, W. Zhao, *Sci. Bull.* **2022**, *67*, 691.
- [38] S. Kasai, S. Sugimoto, Y. Nakatani, R. Ishikawa, Y. K. Takahashi, *Appl. Phys. Express* **2019**, *12*, 083001.
- [39] Y. Guang, L. Zhang, J. Zhang, Y. Wang, Y. Zhao, R. Tomasello, S. Zhang, B. He, J. Li, Y. Liu, J. Feng, H. Wei, M. Carpentieri, Z. Hou, J. Liu, Y. Peng, Z. Zeng, G. Finocchio, X. Zhang, J. M. D. Coey, X. Han, G. Yu, *Adv. Electron. Mater.* **2022**.
- [40] N. E. Penthorn, X. Hao, Z. Wang, Y. Huai, H. W. Jiang, *Phys. Rev. Lett.* **2019**, *122*, 257201.



- [41] X. Zhang, Y. Zhou, M. Ezawa, G. P. Zhao, W. Zhao, *Sci. Rep.* **2015**, 5, 11369.
- [42] G. Chen, A. Mascaraque, A. T. N'Diaye, A. K. Schmid, *Appl. Phys. Lett.* **2015**, 106, 242404.
- [43] P. Ho, A. K. C. Tan, S. Goolaup, A. L. G. Oyarce, M. Raju, L. S. Huang, A. Soumyanarayanan, C. Panagopoulos, *Phys. Rev. Appl.* **2019**, 11, 024064.
- [44] G. Yu, A. Jenkins, X. Ma, S. A. Razavi, C. He, G. Yin, Q. Shao, Q. L. He, H. Wu, W. Li, W. Jiang, X. Han, X. Li, A. C. Bleszynski Jayich, P. K. Amiri, K. L. Wang, *Nano Lett.* **2018**, 18, 980.
- [45] K. G. Rana, A. Finco, F. Fabre, S. Chouaieb, A. Haykal, L. D. Buda-Prejbeanu, O. Fruchart, S. L. Denmat, P. David, M. Belmeguenai, T. Denneulin, R. E. Dunin-Borkowski, G. Gaudin, V. Jacques, O. Boulle, *Phys. Rev. Appl.* **2020**, 13, 044079.
- [46] N. K. Duong, M. Raju, A. P. Petrović, R. Tomasello, G. Finocchio, C. Panagopoulos, *Appl. Phys. Lett.* **2019**, 114, 072401.
- [47] Y.-W. Oh, S.-h. C. Baek, Y. M. Kim, H. Y. Lee, K.-D. Lee, C.-G. Yang, E.-S. Park, K.-S. Lee, K.-W. Kim, G. Go, J.-R. Jeong, B.-C. Min, H.-W. Lee, K.-J. Lee, B.-G. Park, *Nat. Nanotechnol.* **2016**, 11, 878.
- [48] X. Ma, G. Yu, S. A. Razavi, S. S. Sasaki, X. Li, K. Hao, S. H. Tolbert, K. L. Wang, X. Li, *Phys. Rev. Lett.* **2017**, 119, 027202.
- [49] A. Soumyanarayanan, M. Raju, A. L. Gonzalez Oyarce, A. K. C. Tan, M. Y. Im, A. P. Petrovic, P. Ho, K. H. Khoo, M. Tran, C. K. Gan, F. Ernult, C. Panagopoulos, *Nat. Mater.* **2017**, 16, 898.
- [50] A. Maesaka, N. Sugawara, A. Okabe, M. Itabashi, *J. Appl. Phys.* **1998**, 83, 7628.
- [51] J. Jeong, Y. Ferrante, S. V. Faleev, M. G. Samant, C. Felser, S. S. Parkin, *Nat. Commun.* **2016**, 7, 10276.
- [52] M. Tsunoda, K.-i. Imakita, M. Naka, M. Takahashi, *J. Magn. Magn. Mater.* **2006**, 304, 55.
- [53] N. P. Aley, K. O'Grady, *J. Appl. Phys.* **2011**, 109, 07D738.
- [54] Z. Zhu, G. Wu, Y. Ren, S. Lou, Q. Y. Jin, Z. Zhang, *Appl. Phys. Lett.* **2020**, 116, 182407.
- [55] M. Tang, B. Zhao, W. Zhu, Z. Zhu, Q. Y. Jin, Z. Zhang, *ACS Appl. Mater. Interfaces* **2018**, 10, 5090.
- [56] J. Wei, C. He, X. Wang, H. Xu, Y. Liu, Y. Guang, C. Wan, J. Feng, G. Yu, X. Han, *Phys. Rev. Appl.* **2020**, 13, 034041.
- [57] J. B. S. Mendes, R. O. Cunha, O. Alves Santos, P. R. T. Ribeiro, F. L. A. Machado, R. L. Rodríguez-Suárez, A. Azevedo, S. M. Rezende, *Phys. Rev. B* **2014**, 89, 140406.
- [58] W. Skowroński, Ł. Karwacki, S. Ziętek, J. Kanak, S. Łazarski, K. Grochot, T. Stobiecki, P. Kuświk, F. Stobiecki, J. Barnaś, *Phys. Rev. Appl.* **2019**, 11, 024039.
- [59] O. Hellwig, A. Berger, J. B. Kortright, E. E. Fullerton, *J. Magn. Magn. Mater.* **2007**, 319, 13.
- [60] B. Kaplan, G. A. Gehring, *J. Magn. Magn. Mater.* **1993**, 128, 111.
- [61] C. Kittel, *Phys. Rev.* **1946**, 70, 965.
- [62] S. D. Pollard, J. A. Garlow, J. Yu, Z. Wang, Y. Zhu, H. Yang, *Nat. Commun.* **2017**, 8, 14761.
- [63] Y. Guang, Y. Peng, Z. Yan, Y. Liu, J. Zhang, X. Zeng, S. Zhang, S. Zhang, D. M. Burn, N. Jaouen, J. Wei, H. Xu, J. Feng, C. Fang, G. van der Laan, T. Hesjedal, B. Cui, X. Zhang, G. Yu, X. Han, *Adv. Mater.* **2020**, 32, 2003003.